THE UNIVERSITY of EDINBURGH

Edinburgh Research Explorer

Dual-Targeted Multifunctional Nanoparticles for Magnetic Resonance Imaging Guided Cancer Diagnosis and Therapy

Citation for published version:
Nan, X, Zhang, X, Liu, Y, Zhou, M, Chen, X & Zhang, X 2017, 'Dual-Targeted Multifunctional Nanoparticles for Magnetic Resonance Imaging Guided Cancer Diagnosis and Therapy', *ACS Applied Materials & Interfaces*, vol. 9, no. 11, pp. 9986–9995. https://doi.org/10.1021/acsami.6b16486

Digital Object Identifier (DOI):
10.1021/acsami.6b16486

Link:
Link to publication record in Edinburgh Research Explorer

Document Version:
Peer reviewed version

Published In:
ACS Applied Materials & Interfaces

General rights
Copyright for the publications made accessible via the Edinburgh Research Explorer is retained by the author(s) and / or other copyright owners and it is a condition of accessing these publications that users recognise and abide by the legal requirements associated with these rights.

Take down policy
The University of Edinburgh has made every reasonable effort to ensure that Edinburgh Research Explorer content complies with UK legislation. If you believe that the public display of this file breaches copyright please contact openaccess@ed.ac.uk providing details, and we will remove access to the work immediately and investigate your claim.

Download date: 23. Jul. 2021

Dual-Targeted Multifunctional Nanoparticles for Magnetic Resonance Imaging Guided Cancer Diagnosis and Therapy

Xueyan Nan,[†] *Xiujuan Zhang,*[*,†] *Yanqiu Liu,*[†] *Mengjiao Zhou,*[†] *Xianfeng Chen,*[*,‡] *and Xiaohong Zhang*[*,†]

[†]Institute of Functional Nano & Soft Materials (FUNSOM) and Jiangsu Key Laboratory for Carbon-Based Functional Materials & Devices, Soochow University, Suzhou Jiangsu, 215123 (P. R. China).

[‡]Institute for Bioengineering, School of Engineering, University of Edinburgh, Edinburgh EH9 3JL, United Kingdom.

Keywords: multifunctional nanocomposite; dual-target; magnetic resonance imaging; photothermal; chemotherapy

ABSTRACT

Hybrid nanostructures with combined functionalities can be rationally designed to achieve synergistic effects for efficient cancer treatment. Herein, a multifunctional nano-platform is constructed, containing an inner core of an anticancer drug MTX surrounding by a nanometer-thin layer of gold as the shell with Fe_3O_4 magnetic nanoparticles (NPs) evenly distributed in the gold layer, and the outermost hybrid LA-PEG-MTX molecules as surface coating agent (denoted as MFG-LPM NPs). This nanocomposite possesses very high drug loading capacity as the entire core is MTX and integrates magnetic- and active- targeting drug delivery, light-controlled drug release, magnetic resonance imaging (MRI), as well as photothermal and chemotherapy. With a strong near-infrared (NIR) absorbance at 808 nm, the nanocomposite enables temperature elevation and light-triggered MTX release. *In vitro* cytotoxicity studies indicate that the strategy of combining therapy leads to a synergistic effect with high cancer cell killing efficacy. In consistency with this, due to the high accumulation of MFG-LPM NPs at tumor site and their combinatorial chemo-photothermal effects, 100% *in vivo* tumor elimination can be achieved. Additionally, *in vivo* MRI of tumor-bearing mice demonstrates an impressive performance of MFG-LPM NPs as a T_2 contrast agent. Therefore, such multifunctional nanocomposite has the potential to serve as an excellent theranostic agent that collectively integrates multiple functions for efficient MRI guided cancer diagnosis and treatment.

1. INTRODUCTION

The advancement of multifunctional hybrid nanostructures for cancer diagnosis and treatment has attracted continuously increasing attention in the field of nanotechnology and biomedicine.[1-7] For example, researchers have demonstrated that the combinatorial photothermal and chemotherapy can greatly improve the efficacy of cancer treatment and has the potential to overcome drug resistance.[8-10] Photothermal therapy (PTT) is an approach to employ photothermal agents with a strong absorbance in the near-infrared (NIR) region to produce heat to kill target cells with minimal side effects. During last decades, a wide range of PTT agents such as gold nanomaterials (e.g., gold nanorods, nanocages, and nanoshells),[11-15] carbon nanomaterials (e.g., carbon nanotubes, and graphene)[16-20] and many other materials (e.g., polydopamine, poly(4-styrenesulfonate), and indocyanine green (ICG))[21-22] have been widely explored. Chemotherapy is to use drugs to destroy cancer cells. For instance, methotrexate (MTX) has been commonly used in chemotherapy because the similarity of its molecule structure with folic acid lends itself an ability to combine with the overexpressed folate receptor on the surface of many types of cancer cells to effectively kill them.[23] For combinatorial therapy, Kim *et al* have previously demonstrated that, when MTX is combined with photothermal therapy for rheumatoid arthritis, the therapeutic efficacy of 0.05% dosage of MTX is comparable to that of the treatment with a full dose.[24] In using nanotechnology for these therapies, it is convenient to add different functions like surface modifying nanostructures with tumor recognizing ligands or guiding nanomaterials' movement under magnetic field to realize specific targeting to cancer. Beyond combination of these characteristics for therapy, if the nanostructures can be imaged, additional

advantages will be realized as imaging is able to localize tumors, thereby precisely positioning laser irradiation for photothermal therapy, and enabling to monitor tumor development for determining subsequent therapy.[25-26] This is very useful in further improving the efficacy of cancer treatment and meanwhile minimizing any potential negative effect.[27-29] Each of these designs has its merit and the combination is capable of generating synergistic effect. Therefore, it is highly desirable to construct a multifunctional theranostic agent in one single nanosystem to achieve the comprehensive advantages of nanotechnology for efficient cancer treatment and early diagnosis.

To fulfill this goal, it is important to carry out a rational design by identifying suitable imaging mode, therapeutics, and cancer targeting strategies. Among many imaging techniques, MRI has been widely used in clinic owing to its capacity of attaining 3D high-resolution images of living bodies and great imaging depth.[30] To further improve the imaging quality, iron oxide nanoparticles (IONP) are often utilized as a T_2 contrast agent.[31] IONP has also been reported to achieve regulated drug release and targeted drug delivery under magnetic field.[32] For photothermal therapy, gold nanostructures have been extensively researched due to their strong absorption in the first biological window (e.g., 808 nm), high photothermal conversion efficiency, and great biocompatibility.[33] For chemotherapy, MTX can be directly self-assembled to the form of NPs without needing additional nanomaterials as a drug carrier, thereby achieving high drug load and potentially better safety profile. With these rationales, we developed a multifunctional nano-platform containing an inner core of MTX surrounding by a

nanometer-thin layer of gold as the shell with Fe_3O_4 magnetic NPs evenly distributed in the gold layer, and the outermost hybrid LA-PEG-MTX molecules as surface coating (**Scheme 1**). Such architecture represents a nano-platform that can collectively achieve magnetic- and active- targeted drug delivery, light-controlled drug release, MRI, photothermal therapy and chemotherapy for efficient cancer treatment. In this work, we have prepared this nano-platform, systematically investigated their physical and chemical properties, pharmacokinetics, and *in vivo* biodistribution, as well as tested their application for MRI, *in vitro* cell killing, and *in vivo* anticancer therapy.

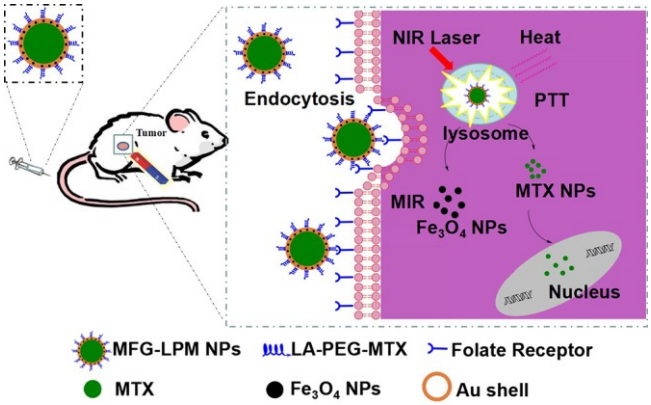

Scheme 1. MFG-LPM NPs are accumulated in tumor site *via* magnetic field guided targeting and surface ligands driven targeting and then internalized by folic acid-receptor mediated endocytosis. Subsequently, NIR illumination is employed to generate heat for photothermal therapy and trigger the release of MTX for chemotherapy and iron oxide NPs for MRI.

2. RESULTS AND DISCUSSION

2.1. Preparation and Characterization of MFG-LPM NPs

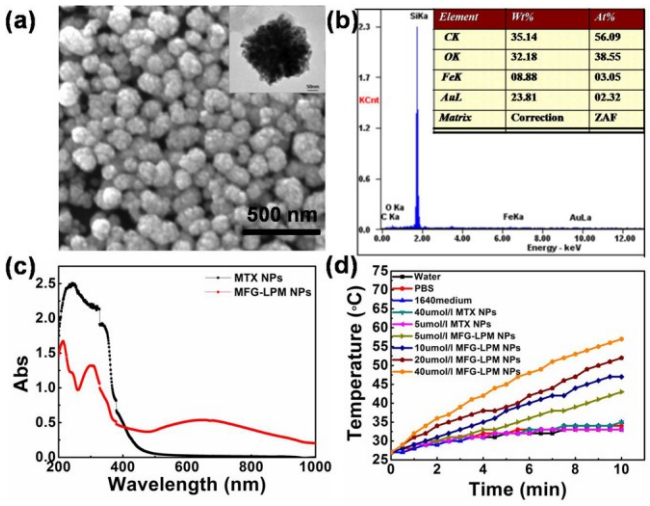

Figure 1. Characterization of MFG-LPM NPs. (a) SEM image of MFG-LPM NPs. Inset: TEM image of an individual MFG-LPM NP. (b) EDX of MFG-LPM NPs under the SEM pattern. (c) UV-vis-NIR absorption spectra of MTX NPs and MFG-LPM NPs. (d) Time-dependent temperature changes of MFG-LPM NPs at different concentrations (5, 10, 20 and 40 μmol/L) under irradiation of a 808 nm laser with a power density of 1 W/cm^2 (standard laser illumination condition in all experiments unless otherwise stated). Water, PBS, 1640 medium and MTX NPs groups were used as references.

The synthesis of multifunctional NPs involved a multistep process. MTX NPs, the core of our designed nanocomposite, were prepared by a solvent exchange method. The digital image of a MTX NP suspension in water is shown in **Figure S1**. These NPs are negatively charged and have an average diameter of about 180 nm, as indicated by their scanning electron microscopy (SEM) image presented in **Figure S2**. The NPs were then surface functionalized with a cationic polymer poly(allylamine hydrochloride) (PAH) (M.W.: 15 kDa) by electrostatic interaction to obtain a positively charged surface (**Figure S3**). This positive charge was made use to conjugate negatively charged Fe_3O_4 NPs and gold nanoseeds on their surface through electrostatic attraction. Subsequently,

hydroxylamine hydrochloride (NH_2OH•HCl) was introduced to reduce the gold precursor chloroauric acid ($HAuCl_4$) to form Au nanoshell on the surface of the nanocomposite. **Figure S3** gives the values of the zeta-potential of different NPs at each stage of the preparation. Upon the modification of PAH to the initial negatively charged MTX NPs, the zeta potential switches from -3.42 to +34.76 mV. After the sequential conjugation of Fe_3O_4 NPs and gold nanoseeds on the surface of PAH-coated MTX NPs, the values of zeta potential of the nanostructures were respectively measured as +13.12 and -0.59 mV. The evolution of the values of the zeta potentials demonstrates the successful alternating deposition of PAH, Fe_3O_4 NPs and gold nanoseeds. Representative SEM and transmission electron microscopy (TEM) images are displayed in **Figure 1a** and these reveal the successful preparation of the nanocomposite containing MTX core and Fe_3O_4 magnetic NPs and gold shell encapsulation (denoted as MFG NPs). The shell structure of MFG NPs can be confirmed by a high-angle annular dark field scanning TEM (HAADF-STEM) image in **Figure S4a**. The line profiles of the elemental composition determined by energy-dispersive X-ray spectroscopy (EDX) and TEM elemental mapping image indicate the presence of Fe and gold (**Figure 1b** and **S4b**). At the end, to improve their water dispersity, biocompatibility, bioavailability, and specific targeting to folate receptor overexpressed cancer cells (**Figure S5**), the as-prepared MFG NPs were functionalized by LA-PEG-MTX through gold-thiol bonds (referred to MFG-LPM NPs) (**Figure S6-8**).[34,35] The final NPs display a hydrodynamic diameter of approximately 188 nm and possess high stability (**Figure S9** and **S10**). During the synthesis process, the surface

plasmon resonance (SPR) peak of MTX NPs is broadened and significantly shifts to longer wavelengths after the formation of gold nanoshell on the surface (**Figure 1c**). This finding is consistent with previous reports involving similar Au nanoshells.[36] It suggests that a rather thin gold nanoshell have been successfully established on the surface of the nanocomposite. It is known that SPR can transform the energy of absorbed laser light to heat.[37] To investigate the influence of NIR laser irradiation on the temperature elevation, 3.0 mL of different concentrations of MFG-LPM NPs were placed in quartz cells and exposed to a 808 nm laser. Meanwhile, the temperature increase of water, PBS, RPMI 1640 medium and MTX NPs suspension was also studied for comparison. Evidently, the MFG-LPM NP suspensions lead to fast increase of temperature with extended irradiation time, while the control groups yield significantly smaller temperature changes. Moreover, a clear dose-dependent temperature increase profile is explored in the groups of MFG-LPM NPs from the figure. With the concentration of NPs increases from 5, 10, 20 to 40 μmol/L, the temperature increases by 16, 20, 25 and 30 °C, respectively (**Figure 1d**). These data indicate that MFG-LPM NPs can readily rise the temperature of samples to above 47 °C and therefore have a great photothermal effect upon irradiation with NIR laser.

2.2. Fast Release of MTX from MTX-LPM NPs Triggered by NIR Light

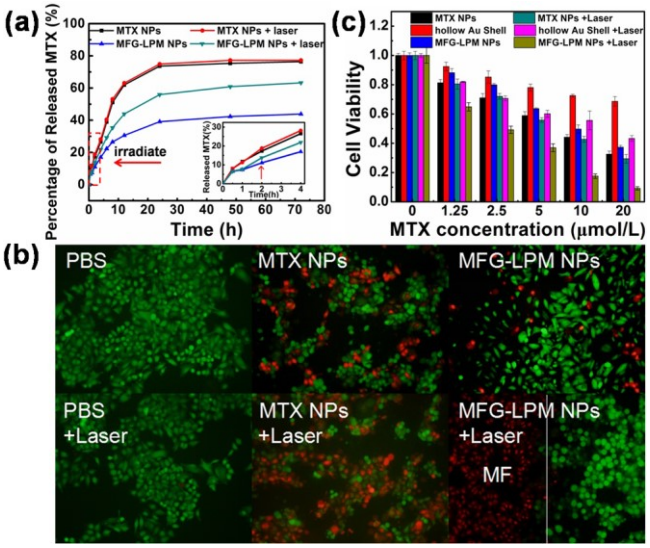

Figure 2. (a) The time-dependent release profiles of free MTX from MTX NPs and MFG-LPM NPs with and without laser illumination. The red arrow indicates the onset of NIR irradiation. (b) Fluorescence microscopy images of KB cells after being treated with PBS, MTX NPs and MFG-LPM NPs under different conditions. The cells were double stained with calcein AM (green signal: living cells) and PI (red signal: dead cells). MF stands for magnetic field. (c) The viabilities of 4T1 cells at 48 h after incubation with a series of concentrations of different groups of NPs with and without NIR laser irradiation.

Figure 2a shows the time-dependent release profiles of free MTX from MTX NPs and MFG-LPM NPs with or without irradiation by a laser. It is clear that the release of MTX from MFG-LPM NPs is the lowest among the four groups in the case of without laser irradiation. The reason may be that the outer Au nanoshell is able to confine MTX within the core of the nanocomposite. This will prevent quick liberation of MTX when the nanocomposite is in blood circulation after systemic delivery, thereby reducing the side effect and enabling high drug accumulation in tumor tissues. In comparison, with

NIR laser irradiation (starting at the time point of "2 h") for 10 min, an abrupt drug release is observed from MFG-LPM NPs, while the release of MTX from MTX NPs does not change with the same treatment. The released percentage of MTX from MFG-LPM NPs increases by approximately 20% over the 3-day observation period when compared with the case of no NIR laser irradiation. A possible explanation is that MFG-LPM NPs can strongly absorb NIR light and transform the energy to local temperature elevation, which in turn promotes the motion of MTX molecules and leads to enhanced MTX release.[38]

2.3. In Vitro Chemo-Photothermal Combination Therapy

To evaluate the efficacy of the dual-targeted photothermal cancer ablation of our designed NPs, different groups of KB cells were treated with MTX NPs, hollow Au nanoshells, MFG-LP NPs (multifunctional nanocomposite with LA-PEG surface coating), and MFG-LPM NPs (multifunctional nanocomposite with LA-PEG-MTX surface coating) with the same MTX concentration for 12 h, and then irradiated by a laser. For the group of hollow Au nanoshells, the Au amount remained the same as that in other groups. To enable magnetic field-aided targeted delivery of nanomedicine, a magnet was placed next to part of cells during experiments. A separate group of KB cells incubated with PBS solution was also studied for comparison. After laser irradiation, all groups of cells were further incubated for 12 h at 37 °C. Subsequently, the cells were stained with Calcine AM and propidium iodide (PI) to mark living (green) and dead (red) cells, respectively**.** For the two PBS groups with and without laser illumination, vast majority of cells is alive (**Figure 2b**). This reveals that the used

laser power is not sufficient to damage cells. In comparison, it is appealing to find that almost all cells incubated with MFG-LPM NPs are killed in the group with NIR light irradiation, while the cells in other groups are only partially killed after incubation, even in the case of under laser irradiation (**Figure S11**). More attractively, because of the localized accumulation of MFG-LPM NPs induced by the applied magnetic field, only the cells nearby the magnet are effectively ablated. There are no dead cells in the other field. The reason is that almost all MFG-LPM NPs are transferred to the area with applied magnetic field and there is negligible amount in the other side (**Figure 2b**).

For systematic quantitative assessment of the drug efficacy of our NPs, we investigated their cell killing capacity when incubate with three cell lines (KB, 4T1 and MRC-5). KB, 4T1 and MRC-5 cells were individually treated with different concentrations of MTX NPs, hollow Au nanoshells and MFG-LPM NPs for 24, 48 and 72 h. As presented in **Figure 2c** and **S12-14**, for all three types of cells, MFG-LPM NPs show time- and dose-dependent toxicities. Among the tested samples, hollow Au nanoshells display the least toxicity in the case of without NIR irradiation. In comparison, when NIR laser is applied, the cell viabilities dramatically decreased, implying the photothermal ablation capability of Au nanoshells. When there is no laser irradiation, MFG-LPM NPs exhibit much lower toxicities than MTX NPs at the same drug concentrations. This can be ascribed to the encapsulation of Au nanoshells on the surface of MTX NPs, which inhibits the release of MTX from MFG-LPM NPs. In great contrast, if with NIR laser illumination, a distinct toxicity is observed with the evidence of the death of most cancer cells at 72 h for MFG-LPM NPs. By overall comparison

among all groups, it is worth noting that the cell-killing efficiency of MFG-LPM NPs is tremendously increased comparing with single photothermal therapy using hollow Au nanoshells or chemotherapy with MTX NPs, proving the enhanced antitumor effect of combinational chemo-photothermal therapy. These observations reveal that the combination of photothermal and chemotherapy in MFG-LPM NPs enables their significantly enhanced therapeutic efficacy.

2.4. In Vivo Blood Circulation and Biodistribution of MFG-LPM NPs

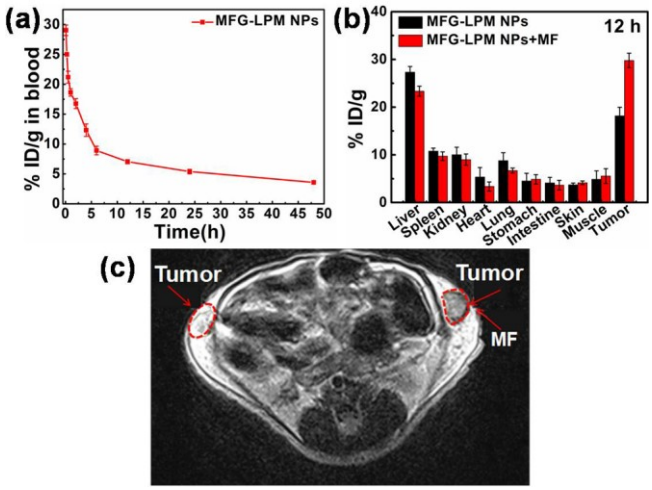

Figure 3. (a) The evolution of the concentration of MFG-LPM NPs in blood circulation after intravenous injection. The unit is a percentage of injected dose per gram tissue (% ID g^{-1}). (b) Biodistribution of MFG-LPM NPs in mice at 12 h after intravenous injection. (c) *In vivo* MRI of tumors (the right side tumor was applied with a magnetic field (MF), but the left side tumor experienced no MF).

To investigate the *in vivo* behaviors of MFG-LPM NPs, we firstly studied their pharmacokinetics. MFG-LPM NPs were administered to BALB/c mice through intravenous injection and the blood samples were collected after different time points. The concentrations of MFG-LPM NPs in blood were determined through measurement

of Au^{3+} by inductively coupled plasma atomic optical emission spectroscopy (ICP-OES). As shown in **Figure 3a**, the half-life of MFG-LPM NPs during blood circulation is approximately 2.9 h. As a comparison, the half-life of MTX free molecules is only 26.5 min.[39] The prolonged blood circulation of MFG-LPM NPs is probably a result of their surface PEG coating and also their particle size. The extended circulation time in blood will favor their accumulation in tumor site through the EPR effect. After studying the blood circulation of MFG-LPM NPs, we also interrogated their *in vivo* biodistribution profiles. In the experiments, 200 μL of MFG-LPM NPs with 0.5 mg/mL MTX were intravenously injected to 4T1 tumor-bearing BALB/c mice and the mice were sacrificed at 2, 6, 12 and 24 h afterwards. Next, three mice's major organs were collected followed by solubilization in aqua regia to determine the concentration of Au^{3+} by ICP-OES. In one group, a magnet was placed next to the tumor to induce improved NP accumulation in the tumor site. The organs of an untreated mouse were used as controls to measure the Au background signal. The results indicate that high levels of MFG-LPM NPs are detected in tumors, liver and spleen in all groups (**Figure 3b** and **S15**). Attractively, the accumulation of MFG-LPM NPs in the tumor with applied magnetic field is constantly higher than others, demonstrating the advantage of combining surface ligands induced active targeting, magnetic field aid targeting, and the passive EPR effect.[40]

Tumor imaging was performed in 4T1 tumor-bearing mice at one day after intravenous injection of MFG-LPM NPs. Firstly we demonstrated the MRI of tumors without magnetic field. As shown in **Figure S16**, the tumors in both right and left sides

show obvious darkening effects in T_2-weighted MRI. Next, to achieve magnetic field-aided targeting, a magnet was placed on the right side tumor of a mouse for 30 min. In this case, due to the magnetic field, majority of the MFG-LPM NPs will be transported to the right side tumor and very low amount is able to reach the left side (similar effect to the experiment shown in **Figure 2b**). Therefore, the tumor in the left side displays very bright signal and the right side exhibits obvious darkening effects in T_2-weighted MRI (**Figure 3c**). These results suggest that MFG-LPM NPs can be simultaneously a contrast agent for MRI and a carrier for magnetic field-aided targeted drug delivery.

2.5. In Vivo Targeted Chemo-Photothermal Therapy

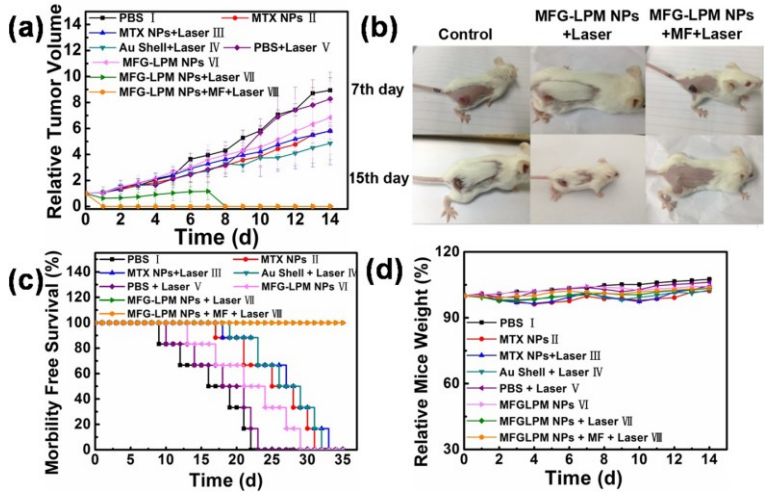

Figure 4. (a) *In vivo* antitumor activities of different treatments on 4T1 tumor bearing BALB/c mice (n = 6 in each group). (b) Representative photos of mice on the 7th and 15th day after injection of different materials for treatment. (c) The survival rate of different groups of mice at different times after treatments. During the experiments, when the tumor volume was over 1000 mm^3, the mouse was withdrawn and considered as death. (d) The evolution of the body weight of mice at different points. The weight was normalized to initial value of each mouse.

The *in vivo* therapeutic efficacy of MFG-LPM NPs was studied using 4T1 tumor bearing BALB/c mice as an animal model. Eight groups of mice (n = 6 in each group) were assessed upon injection of different materials, including: PBS (negative control group) (Group Ⅰ), PEGylated MTX NPs (Group Ⅱ), PEGylated MTX NPs with laser illumination (Group Ⅲ), hollow Au nanoshells with laser illumination (Group Ⅳ), PBS with laser illumination (Group Ⅴ), MFG-LPM NPs (Group Ⅵ), MFG-LPM NPs with laser illumination but without magnetic field (Group Ⅶ), MFG-LPM NPs with laser illumination and magnetic field (Group Ⅷ). The dose of MTX was maintained as 5 mg/Kg in the relevant groups. All mice were administered with two doses on Day 0 and 7, except that those in Group Ⅷ received only one dose on Day 0. For the groups needing laser illumination, on Day 1 and 8 (24 hours after each injection), an NIR laser was used to irradiate the tumors for 10 min. During experiments, the tumor sizes of the mice were measured on daily basis. The results reveal that there is large variation in tumor growth rates among groups. As illustrated in **Figure 4a**, the tumors in Group Ⅰ and Ⅴ (PBS control group and PBS with laser treatment group) rapidly increase with a comparable growth rate. Using Group I as the negative control, the tumor inhibition rate of group Ⅴ is only 7.4%, indicating that the laser irradiation with 1 W/cm^2 power density has negligible influence on tumor growth. In contrast, in the two groups treated with MTX NPs with or without laser illumination, the tumor growth is moderately inhibited, with a similar inhibition rate of about 35.0%. MFG-LPM NPs have lower anticancer effect than both MTX NPs groups (Group Ⅱ and Ⅲ) when there is no laser illumination, showing a tumor inhibition rate of 23.5%. This is in line with the *in*

vitro results and the reason can be ascribed to the Au nanoshell's slowing down the release of MTX from MFG-LPM NPs. It is appealing that a single injection of hollow Au nanoshells is able to partially damage the tumor under NIR illumination (date not shown). With a boost of another injection, the tumor inhibition rate reaches 45.7%. When combining Au nanoshells for photothermal therapy and MTX for chemotherapy in Group Ⅶ (without magnetic field), the tumor growth is significantly inhibited with negligible increase in volume. When a boost injection is given, the tumor can be eliminated (the tumor inhibition rate is 100%). Most attractively, the tumors of the mice in Group Ⅷ can be effectively restrained and ablated only within a short period (the tumor inhibition rate is 100%), in which the mice were administered with MFG-LPM NPs and under the aid of magnetic field and NIR light. At one day after laser illumination, small scars were found on the skin of tumors with a dark gray color, eventually falling off on the 15^{th} day (**Figure 4b**). There was no tumor recurrence during the 35-day experimental period. These findings clearly show that the integrated combination of magnetic- and active- targeted chemotherapy and photothermal treatments in MFG-LPM NPs provides an excellent synergistic effect. All of the mice in the group treated with MFG-LPM NPs and exposed to laser irradiation are able to survive in the whole observation period of 35 days, while the mice in all other groups have life spans from 21 to 34 days (**Figure 4c**).

2.6. In Vivo systematic toxicity

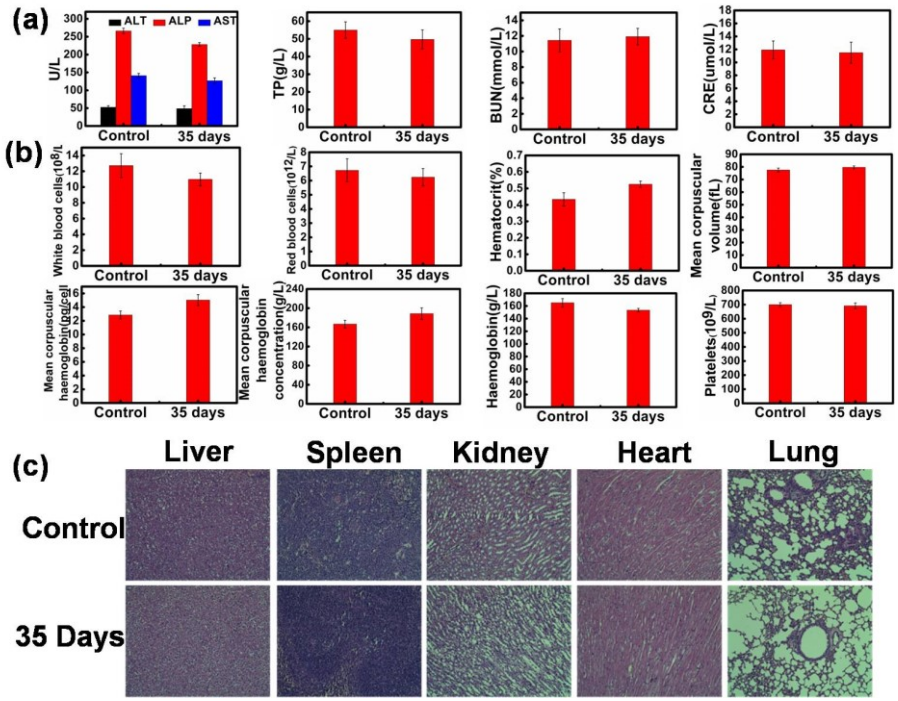

Figure 5. (a) Serum biochemistry data of mice at 35 days after treatment. (b) The complete blood biochemical panel data analysis of mice at 35 days after treatment. The control group was healthy mice. (c) H&E stained organ slices of the mice after 35 days MFG-LPM NPs-based chemo-photothermal treatment.

The *in vivo* toxicity and possible side effects of nanomedicines have to be carefully studied before their potential application in clinic. To verify the applicability of MFG-LPM NPs *in vivo*, we measured the body weight of each mouse on daily basis during the treatment period. It is appealing that there is no dramatic weight loss in all groups (**Figure 4d**). This indicates that our NPs do not possess acute toxicity at the administered dose. Then we carefully monitored the influences of MFG-LPM NPs on BALB/c mice in our experiment. The tumor bearing mice were sacrificed at the end of the treatment (35 days after the first dose) for blood analysis and histological examination (n = 5). The same analysis was also done to age-matched healthy mice for comparison (n = 5). The blood analysis (**Figure 5a**) indicates that no visible hepatic

and kidney disorder is shown in the mice after treatment. Beyond this, the different biological indicators of the treated mice are within normal range (**Figure 5b**). In organ histology, no sign of organ damage and inflammation was observed (**Figure 5c**), suggesting the minimal side effects of MFG-LPM NPs in *in vivo*. The organ coefficients of liver, spleen, kidney, heart and lung in tumor bearing mice are 6.368±0.048%, 0.680±0.074%, 1.622±0.016%, 0.594±0.088% and 0.737±0.063%, respectively, very similar to those in healthy mice. Overall, all of these data evidence that MFG-LPM NPs induce no significant side effect in *in vivo* cancer therapy, demonstrating a significant prospect for efficient and safe cancer therapy in potential clinical applications.

3. CONCLUSION

In summary, we have synthesized MFG-LPM NPs as a multifunctional platform to integrate magnetic- and active- targeted drug delivery, MRI, NIR light-induced drug release and photothermal and chemotherapy into one system. The resulting MFG-LPM NPs have surface plasmon absorbance in the NIR region, thereby enabling NIR-triggered temperature increase and MTX release. Both *in vitro* and *in vivo* studies indicate a synergistic effect in killing cancer cells by the combination of magnetic-field-guided drug delivery and chemo-photothermal therapy. Moreover, *in vivo* MRI of tumor-bearing mice can be attained using MFG-LPM NPs to act as a T_2 contrast agent. Collectively, this smart "all-in-one" nanosystem can serve as a promising theranostic agent for effective cancer diagnosis and therapy, possibly leading to an effective clinical application.

4. EXPERIMENTAL SECTION

4.1. Materials

MTX was purchased from Energy-Chemical (Shanghai, China). Dimethylsulfoxide (DMSO), $FeCl_3$, $FeCl_2 \cdot 4H_2O$, NaOH, ethanol, sodium citrate, sodium borohydride ($NaBH_4$), dichloromethane (CH_2Cl_2), trifluoroacetic acid (TFA), hydroxylamine hydrochloride ($NH_2OH \cdot HCl$), triethylamine (TEA), Triton X-100, sodium dodecylsulphate (SDS), Tris, and potassium carbonate (K_2CO_3) were ordered from Sinopharm Chemical Reagent Co. (China). Poly(allylamine hydrochloride) (PAH), poly(maleic anhydride-alt-1-octadecene) (PMHC18), (α+) Lipoic acid (LA), , 3-(4,5-dimethylthiazol-2-yl)-2,5-diphenyltetrazolium bromide (MTT), hydrogen tetra-chloroaurate (III) hydrate ($HAuCl_4 \cdot 3H_2O$), EDC, and N-hydroxy-succinamide (NHS) were obtained from Sigma Aldrich (Milwaukee, WI). Boc(NH)-PEG-NH_2 was purchased from Suzhou DMD BioMed Ltd. Penicillin-streptomycin solution, Roswell Park Memorial Institute-1640 (RPMI-1640), and Fetal bovine serum (FBS) medium were ordered from Invitrogen (San Diego, CA).

4.2. Characterization

The morphology of NPs were observed by SEM (FEI Quanta 200 FEG) and TEM (FEI Tecnai G2 F20 S-TWIN). The UV-vis absorption spectra of NPs were recorded using a Perkin-Elmer Lambda 750 UV/vis/NIR spectrophotometer. The amount of MTX was assessed from the absorbance of samples at 306 nm. Dynamic light scattering (DLS) analysis was carried out on a Zetasizer Nano ZS (Malvern Instruments, Malvern,

U.K.) to determine the size and zeta potential of NPs. ^{1}H NMR spectra of samples in deuterated solvents were analyzed by a Bruker Avance 400 spectrometer.

4.3. Preparation of MTX NPs

MTX NPs were synthesized through solvent exchange. During the preparation, MTX/DMSO solution (250 μL, 1×10^{-3} M) was dropwisely added to water (5 mL) under vigorous stirring. After 5 min stirring, the sample was incubated at room temperature for 72 hours.

4.4. Synthesis of Fe_3O_4 NPs

Fe_3O_4 NPs were prepared as follows: $FeCl_2 \cdot 4H_2O$ (1.148 g) and $FeCl_3$ (1.057 g) were mixed in water (30 mL) under stirring followed by heating the mixture to 60 °C and keeping for 30 min. Subsequently, this mixture was added to NaOH solution (25 mL, 1 M) to obtain a black-colored mixture. Then more NaOH solution was dropwisely added until the pH value reached 11. Next, sodium citrate (0.248 g) was added and the mixture was heated to and kept at 80 °C for 1 h, followed by cooling to room temperature. The black product was then dissolved in ethanol. The undispersed residue was removed by centrifugation. At the end, these produced Fe_3O_4 NPs were redispersed in distilled water.

4.5. Preparation of Gold NPs

Gold NPs were synthesized by reducing chloroauric acid with sodium boronhydride ($NaBH_4$). Briefly, sodium citrate solution (2 mL, 1.0 wt %) were added to 100 ml of deionized water and stirred for 3 min. Then $HAuCl_4 \cdot 3H_2O$ (1 mL, 1.0 wt %) was added with stirring. Five minutes later, $NaBH_4$ (1 mL, 0.1 wt %) in sodium citrate solution

(1.0 wt %) was promptly injected followed by 15 min reaction to obtain sodium citrate stabilized gold NPs.

4.6. Synthesis of LA-PEG-MTX, C18-PEG-MTX and C18-PEG-FA

We firstly produced Boc(NH)-PEG-LA according to previously reported method.[41] Subsequently, Boc(NH)-PEG-LA was reacted with trifluoroacetic acid (2 mL) for 24 h, followed by drying the reaction solution with nitrogen. The product was placed in 10 mL of water and undergone extraction by CH_2Cl_2. Next, the organic solvent was evaporated and the product was dissolved in water and then lyophilized (termed NH_2-PEG-LA).

For production of MTX-PEG-LA, MTX (45.4 mg) were reacted with NHS (143.7 mg) in DMSO (5 mL) for 1 h the presence of EDC (38.3 mg), and then the mixture was added with NH_2-PEG-LA (250 mg) for reaction of 24 h. At the end, the solution was placed in a dialysis bag (MWCO 5000) for 1-day dialysis followed by filtration and lyophilization. The product was indicated as MTX-PEG-LA.

The synthesis of C18-PEG-MTX and C18-PEG-FA were similar to that of PEG-MTX-LA except that LA and MTX were replaced with C18PMH and FA, respectively, in the reaction.

The chemical structures were confirmed by ^{1}H NMR. Figure S7 and S8 exhibits the ^{1}H NMR spectra of MTX, LA-PEG-NH_2, MTX-PEG-LA, C18PMH-PEG-NH_2, FA, C18PMH-PEG-MTX and C18PMH-PEG-FA. As in the ^{1}H NMR spectra of MTX-PEG-LA, the peaks at 1.86-1.91, 3.5-3.7, and 8.55 ppm are characteristic to LA, PEG and MTX, respectively (Figure S7). As in the ^{1}H NMR spectra of C18PMH-PEG-FA

and C18PMH -PEG-MTX (Figure S8), the peaks at 1.25 and 8.60 are belong to C18PMH and FA, respectively. These results demonstrate the successful conjugation of LA-PEG-MTX, C18PMH-PEG-MTX and C18PMH-PEG-FA.

4.7. Synthesis of MFG-LP and MFG-LPM NPs

MFG-LP and MFG-LPM NPs were synthesized as follows: 80 μL of 1.0 mg/mL of PAH solution was mixed with 4 mL of MTX NPs suspension. The excess volume of PAH was poured off after centrifugation to precipitate the NPs and the NPs were washed with fresh water. Then 200 μL of Fe_3O_4 NPs and gold NPs solution were added to the MTX NP solution with active stirring at room temperature. Subsequently, for growth of a thin layer of gold shell on the surface of these NPs, $HAuCl_4$ (1.5 mL, 1%) was added into water (100 mL) containing K_2CO_3 (25 mg). The solution became colorless after 30 minutes. This solution was then aged for a whole day. Next, 4 mL of the Fe_3O_4 NPs and gold NPs coated MTX NPs dispersion was mixed with 4-6 mL of the aged solution. Following this, NH_2OH•HCl (400 μL, 2 M) was injected. At about 2 minutes after injection, the color of the solution turned from colorless to blue green, and this indicates the formation of gold nanoshell (referred to MFG NPs). LA-PEG and LA-PEG-MTX were then individually added into the mixture solution to surface modify the MFG NPs. At the end, the surface modified NPs were precipitated by centrifugation followed by repeated water washing.

After Au nanoshell was formed on MTX NPs, the product was dispersed in DMSO to remove the core followed by centrifugation to obtain hollow Au nanoshells.

4.8. Release of MTX from MFG-LPM NPs

The release profiles of MTX from MFG-LPM NPs upon NIR laser irradiation were investigated at 37 °C. Two milliliters of MFG-LPM NPs suspension were placed in a dialysis bag (MWCO 5000) and then the bag was immersed into 50 mL of PBS with stirring. After 2 hours, the suspension was exposed to NIR laser irradiation for 10 min. At different time internals, PBS (2 mL) containing liberated MTX were collected. The release pool was replenished with fresh PBS after each sample collection. The amount of the released MTX was measured by determining its absorbance at 306 nm. The experiments were performed in 3 replicates and the average was used in quantitative analysis.

4.9. Temperature elevation by MFG-LPM NPs

Three milliliters of different concentrations of MFG-LPM NPs were placed in quartz cuvettes and then exposed to NIR laser irradiation (808 nm, 1 W/cm^2, 10 min; standard laser irradiation condition unless other stated). The temperature change of each sample was determined at every 30 s by a digital thermometer equipped with a thermocouple probe.

4.10. Cell Culture

Human nasopharyngeal epidermal carcinoma cell line (KB cell), normal human embryonic lung fibroblasts (MRC-5 cell) and murine breast cancer cell line (4T1 cell) were obtained from American Type Culture Collection (ATCC). KB cells, 4T1 cells and MRC-5 cells were cultured in RPMI-1640 medium supplemented with 10% FBS and 1% penicillin/streptomycin at 37 °C in a humidified atmosphere containing 5% of CO_2. The cells were routinely passaged using trypsin (0.05%)/EDTA. For Calcine

AM/PI test, KB cells which grown in FA (-) RPMI-1640 culture medium were cultured in a 35 mm dish for overnight.

4.11. Cytotoxicity Measurement

The *in vitro* cytotoxicity of different materials was determined by the MTT assay. KB, MRC-5 and 4T1 cells were individually seeded into 96-well plates (100 μL per well) followed by incubation for 24 h. Different groups of cells were then treated with different concentrations of MTX NPs, hollow Au nanoshells and MFG-LPM NPs for 24, 48 and 72 h. Some groups of the cells were exposed to NIR laser illumination while other groups were not irradiated by laser. Then the cells were incubated for different periods of time followed by treatment with MTT solution (20 μL, 5 mg/mL in PBS) and incubation for further 4 h. Finally, the medium was vacated and the cells were lysed by adding 150 μL of DMSO for MTT assay to measure the cell viabilities of different groups. The reported data represent the mean values of triplicate measurements.

4.12. Blood Circulation and Biodistribution

Ten microliters of blood were drawn from the tail vein of BALB/c mice at different time points after injection of MFG-LPM NPs. Then the blood samples were solubilized in one milliliter of lysis buffer containing 1% of SDS, 1% of Triton X-100, and 40 mM Tris Acetate. The amount of gold in the samples was measured by ICP-OES. The blood samples from mice without MFG-LPM NPs injection were also analyzed to subtract the background measurement of gold. The concentrations of MFG-LPM NPs in blood circulation at different times are shown as the percentage of injected dose per gram of tissue (% ID/g).

For NP's biodistribution analysis, MFG-LPM NPs were injected to 4T1 tumor-bearing mice (tumor size ~ 100 mm^3) and the mice were terminated at 2, 6, 12 and 24 h after injection. The major organs and tumors of the mice were weighed and solubilized in solutions of HNO_3: HCl: $HClO_4$ with a volume ratio of 3:1:2 followed by heating to 200 °C for 2 h. Then all samples were cooled to room temperature, water was added to each to a final volume of 5 mL. Subsequently, the amount of Au^{3+} in each sample was measured with ICP-OES. Every group has 3 mice. The quantity of MFG-LPM NPs in each organ is expressed with the unit of the percentage of injected dose per gram tissue (% ID g^{-1}).

4.13. In Vivo MRI

A tumor-bearing mouse was intravenously injected with 200 μL of 0.5 mg/mL of MFG-LPM NPs. After injection, the right side tumor was placed under an external magnetic field for 30 min while the left one was not. T_2-weighted MRI was recorded on a 3T clinical MRI scanner (Bruker Biospin Corporation, Billerica, MA, USA) equipped with small animal imaging coil.

4.14. In Vivo Chemo-Photothermal Therapy

The *in vivo* function of MFG-LPM NPs was studied in BALB/c mice bearing 4T1 tumor model. The experiments included 8 groups (n=6 in each group): PBS (Group Ⅰ), PEGylated MTX NPs (Group Ⅱ), PEGylated MTX NPs with laser treatment (Group Ⅲ), hollow Au nanoshells with laser treatment (Group Ⅳ), PBS with laser treatment (Group Ⅴ), MFG-LPM NPs (Group Ⅵ), MFG-LPM NPs with laser treatment but without magnetic field (Group Ⅶ), MFG-LPM NPs with laser treatment and magnetic

field (Group Ⅷ). The dose of MTX was maintained as 5 mg/Kg in the relevant groups. The mice received two injections on day 0 and 7, except that the mice in Group Ⅷ had only one injection on day 0. At 24 h after each injection, an NIR laser was employed to irradiate tumors in Group Ⅲ, Ⅳ, Ⅴ, Ⅶ and Ⅷ. In the experimental period, the tumor dimensions and mouse weight were measured on daily basis. The tumor volume was calculated using the formula $a \times b^2/2$, where a is the largest and b the smallest diameter. The tumor volume and mouse body weight were normalized in comparison with their initial values. The organ coefficient was calculated with formula of organ weight / (body weight – tumor weight).

4.15. In Vivo Systematic Toxicity

After 35 days treatment, five mice from Group Ⅷ were sacrificed and blood samples and major organs and tissues including liver, spleen, kidney, heart, lung, intestine, stomach, skin, and muscle were collected. Five age-matched mice were used as a control group. Then the major organs and tissues were fixed in 10% neutral buffered formalin, processed routinely into paraffin, and sectioned to samples with 8 μm in thickness for hematoxylin and eosin (H&E) staining. The stained samples were examined under digital microscopy (Leica QWin).

ASSOCIATED CONTENT

Supporting Information

Photographs of different NPs, SEM image of MTX NPs. Zeta-potential of nanostructures at different stages during the preparation of MFG-LPM NPs. HRTEM image of a thin gold shell grown on the surface of MTX core NPs and STEM image

and HAADF-STEM-EDS mapping images of MFG-LPM NPs. FTIR and ^{1}H NMR spectra of MTX, LA-PEG-NH_2 and LA-PEG-MTX. ^{1}H NMR spectra of C18PMH-PEG-NH_2, FA, C18PMH-PEG-FA and C18PMH-PEG-MTX. Size distribution of MTX NPs and MFG-LPM NPs. Photographs of MFG-LPM NPs and MFG NPs immediate after preparation, and at 3 days after preparation. Fluorescence microscopy images of KB cells after being treated with hollow Au shell, MFG-LA-PEG NPs and MFG-LPM NPs under different conditions and co-stained with calcein AM and PI to indicate living and dead cells. Cell viabilities of 4T1 cells, KB cells and MRC-5 cells treated with different conditions for different periods. Biodistribution of MFG-LPM NPs in mice for various periods.This material is available free of charge via the Internet at http://pubs.acs.org.

AUTHOR INFORMATION

Corresponding Author

* (X. J. Z.) Tel: +86-512-65880955. E-mail: xjzhang@suda.edu.cn;

* (X. H. Z.) Tel: +86-512-65880631. E-mail: xiaohong_zhang@suda.edu.cn;

* (X. C.) E-mail: xianfeng.chen@oxon.org.

Author Contributions

Xueyan Nan and Yanqiu Liu had the same contribution to this work. All authors contributed to the manuscript writing and approved the final version of the manuscript.

Notes

The authors declare no competing financial interest.

ACKNOWLEDGMENT

This work was supported by the National Basic Research Program of China [2013CB933500], National Natural Science Foundation of China [Grant numbers 61422403, 51672180, 51622306, 21673151], the Priority Academic Program Development of Jiangsu Higher Education Institutions (PAPD), Qing Lan Project, and Collaborative Innovation Center of Suzhou Nano Science and Technology (NANO-CIC).

REFERENCES

(1) Hu, S. H. and Gao, X. Nanocomposites with Spatially Separated Functionalities for Combined Imaging and Magnetolytic Therapy. *J. Am. Chem. Soc.* **2010**, *132*, 7234-7237.

(2) Kim, D.; Jeong, Y. Y.; Jon, S. A Drug-Loaded Aptamer-Gold Nanoparticle Bioconjugate for Combined CT Imaging and Therapy of Prostate Cancer. *ACS Nano* **2010**, *4*, 3689-3696.

(3) Lee, J. E.; Lee, N.; Kim, T.; Kim, J.; Hyeon, T. Multifunctional Mesoporous Silica Nanocomposite Nanoparticles for Theranostic Applications. *Acc. Chem. Res.* **2011**, *44*, 893-902.

(4) Wang, J.; Zhu, G. Z.; You, M. X.; Song, E.; Shukoor, M. I.; Zhang, K. J.; Altman, M. B.; Chen, Y.; Zhu, Z.; Huang, C. Z.; Tan, W. H. Assembly of Aptamer Switch Probes and Photosensitizer on Gold Nanorods for Targeted Photothermal and Photodynamic Cancer Therapy. *ACS Nano* **2012**, *6*, 5070-5077.

(5) Huang, P.; Lin, J.; Wang, X. S.; Wang, Z.; Zhang, C. L.; He, M.; Wang, K.; Chen, F.; Li, Z. M.; Shen, G. X.; Cui, D. X.; Chen, X. Y. Light-Triggered Theranostics Based on Photosensitizer-Conjugated Carbon Dots for Simultaneous Enhanced-Fluorescence Imaging and Photodynamic Therapy. *Adv. Mater.* **2012**, *24*, 5104-5110.

(6) Zheng, M. B.; Yue, C. X.; Ma, Y. F.; Gong, P.; Zhao, P. F.; Zheng, C. F.; Sheng, Z. H.; Zhang, P. F.; Wang, Z. H.; Cai, L. T. Single-Step Assembly of DOX/ICG Loaded Lipid Polymer Nanoparticles for Highly Effective Chemo-Photothermal Combination Therapy. *ACS Nano* **2013**, *7*, 2056-2067.

(7) Wang, J.; Zhu, G. Z.; You, M. X.; Song, E.; Shukoor, M. I.; Zhang, K. J.; Altman, M. B.; Chen, Y.; Zhu, Z.; Huang, C. Z.; Tan, W. H. Assembly of Aptamer Switch Probes and Photosensitizer on Gold Nanorods for Targeted Photothermal and Photodynamic Cancer Therapy. *ACS Nano* **2012**, *6*, 5070-5077.

(8) Zhang, J. F.; Liang, Y. C.; Lin, X. D.; Zhu, X. Y.; Yan, L.; Li, S.; Yang, X.; Zhu, G. Y.; Rogach, A. L.; Yu, P. K.; Shi, P.; Tu, L. C.; Chang, C. C.; Zhang, X. H.; Chen, X. F.; Zhang, W. J.; Lee, C. S. Self-Monitoring and Self-Delivery of Photosensitizer-Doped Nanoparticles for Highly Effective Combination Cancer Therapy *in Vitro* and *in Vivo*. *ACS Nano* **2015**, *9*, 9741-9756.

(9) Chen, R.; Zhang, J. F.; Wang, Y.; Chen, X. F.; Zapien, J. A.; Lee, C. S. Graphitic Carbon Nitride Nanosheet@metal–Organic Framework Core–Shell Nanoparticles for Photo-Chemo Combination Therapy. *Nanoscale* **2015**, *7*, 17299-17305.

(10) Wang, Z. G.; Ma, R.; Yan, L.; Chen, X. F.; Zhu, G. Y. Combined Chemotherapy and Photodynamic Therapy Using a Nanohybrid Based on Layered Double Hydroxides to Conquer Cisplatin Resistance. *Chem. Commun.* **2015**, *51*, 11587-11590.

(11) Yavuz, M. S.; Cheng, Y. Y.; Chen, J. Y.; Cobley, C. M.; Zhang, Q.; Rycenga, M.; Xie, J. W.; Kim, C. H.; Song, K. H.; Schwartz, A. G.; Wang, L. V.; Xia, Y. N. Gold Nanocages Covered by Smart Polymers for Controlled Release with Near-Infrared Light. *Nat. Mater.* **2009**, *8*, 935-939.

(12) Xiao, Z. Y.; Ji, C. W.; Shi, J. J.; Pridgen, E. M.; Frieder, J.; Wu, J.; Farokhzad, O. C. DNA Self-Assembly of Targeted Near-Infrared-Responsive Gold Nanoparticles for Cancer Thermo-Chemotherapy. *Angew. Chem. Int. Ed.* **2012**, *51*, 1-6.

(13) Li, W.; Zhang, X. J.; Zhou, M. J.; Tian, B. S.; Yu, C. T.; Jie, J. S.; Hao, X. J.; Zhang, X. H. Functional Core/Shell Drug Nanoparticles for Highly Effective Synergistic Cancer Therapy. *Adv. Healthcare Mater.* **2014**, *3*, 1475-1485.

(14) Chen, J. Y.; Yang, M. X.; Zhang, Q.; Cho, E. C.; Cobley, C. M.; Kim, C.; Glaus, C.; Wang, L. V.; Welch, M. J.; Xia, Y. M. A Novel Class of Multifunctional Nanomaterials for Theranostic Applications. *Adv. Funct. Mater.* **2010**, *20*, 3684-3694.

(15) Ma, Y.; Liang, X. L.; Tong, S.; Bao, G.; Ren, Q. S.; Dai, Z. F. Gold Nanoshell Nanomicelles for Potential Magnetic Resonance Imaging, Light-Triggered Drug Release, and Photothermal Therapy. *Adv. Funct. Mater.* **2013**, *23*, 815-822.

(16) Kam, N. W. S.; O'Connell, M.; Wisdom, J. A.; Dai, H. Carbon Nanotubes as Multifunctional Biological Transporters and Near-Infrared Agents for Selective Cancer Cell Destruction. *Proc. Natl. Acad. Sci. U.S.A.* **2005**, *102*, 11600-11605.

(17) Robinson, J. T.; Tabakman, S. M.; Liang, Y.; Wang, H.; Casalongue, H. S.; Vinh, D.; Dai, H. Ultrasmall Reduced Graphene Oxide with High Near-Infrared Absorbance for Photothermal Therapy, *J. Am. Chem. Soc.* **2011**, *133*, 6825-6831.

(18) Chen, Y. W.; Chen, P. J.; Hu, S. H.; Chen, I. W.; Chen, S. Y. NIR-Triggered Synergic Photo-chemothermal Therapy Delivered by Reduced Graphene Oxide/Carbon/Mesoporous Silica Nanocookies. *Adv. Funct. Mater.* **2014**, *24*, 451-459.

(19) He, Q. J.; Kiesewetter, D. O.; Qu, Y.; Fu, X.; Fan, J.; Huang, P.; Liu, Y. J.; Zhu, G. Z.; Liu, Y.; Qian, Z. Y.; Chen, X. Y. NIR-Responsive On-Demand Release of CO from Metal Carbonyl-Caged Graphene Oxide Nanomedicine. *Adv. Mater.* **2015**, *27*, 6741-6746.

(20) Zhang, Y.; Cui, Z. F.; Kong, H. T.; Xia, K.; Pan, L.; Li, J.; Sun, Y. H.; Shi, J. Y.; Wang, L. H.; Zhu, Y.; and Fan, C. H. One-Shot Immunomodulatory Nanodiamond Agents for Cancer Immunotherapy. *Adv. Mater.* **2016**, *28*, 2699-2708.

(21) Lin, L. S.; Cong, Z. X.; Cao, J. B.; Ke, K. M.; Peng, Q. L.; Gao, J. h.; Yang, H. H.; Liu, G.; Chen, X. Y. Multifunctional Fe_3O_4@Polydopamine Core/Shell Nanocomposites for Intracellular mRNA Detection and Imaging-Guided Photothermal Therapy. *ACS Nano* **2014**, *8*, 3876-3883.

(22) Yang, Y. L.; Zhang, X. J.; Yu, C. T.; Hao, X. J.; Jie, J. S.; Zhou, M. J.; Zhang, X. H. Smart Nanorods for Highly Effective Cancer Theranostic Applications. *Adv. Healthcare Mater.* **2014**, *3*, 906-916.

(23) Li, M. H.; Choi, S. K.; Thomas, T. P.; Desai, A.; Lee, K. H.; Kotiyar, A.; Holl, M. M. B.; James, R.; Baker, J. Dendrimer-based Multivalent Methotrexates as Dual

Acting Nanoconjugates for Cancer Cell Targeting. *Eur. J. Med. Chem.* **2012**, *47*, 560-572.

(24) Kim, H. J.; Lee, S. M.; Park, K. H.; Mun, C. H.; Park, Y. B.; Yoo, K. H. Drug-loaded Gold/iron/gold Plasmonic Nanoparticles for Magnetic Targeted Chemo-Photothermal Treatment of Rheumatoid Arthritis. *Biomaterials* **2015**, *61*, 95-102.

(25) Sheng, Z. H.; Hu, D. H.; Zheng, M. B.; Zhao, P. F.; Liu, H. L.; Gao, D. Y.; Gong, P.; Gao, G. H.; Zhang, P. F.; Ma, Y. F.; Cai, L. T. Smart Human Serum Albumin-Indocyanine Green Nanoparticles Generated by Programmed Assembly for Dual-Modal Imaging-Guided Cancer Synergistic Phototherapy. *ACS Nano* **2014**, *8*, 12310-12322.

(26) Xie, J.; Lee, S.; Chen, X. Nanoparticle-Based Theranostic Agents Review. *Adv. Drug Delivery Rev.* **2010**, *62*, 1064-1079.

(27) Chapman, S.; Dobrovolskaia, M.; Farahani, K.; Goodwin, A.; Joshi, A.; Lee, H.; Meade, T.; Pomper, M.; Ptak, K.; Rao, J. H.; Singh, R.; Sridhar, S.; Stern, S.; Wang, A.; Weaver, J. B.; Woloschak, G.; Yang, L. Nanoparticles for Cancer Imaging: The Good, the Bad, and the Promise. *Nano Today* **2013**, *8*, 454-460.

(28) Liang, X. L.; Li, Y. Y.; Li, X. D.; Jing, L. J.; Deng, Z. J.; Yue, X. L.; Li, C. H.; Dai, Z. F. PEGylated Polypyrrole Nanoparticles Conjugating Gadolinium Chelates for Dual-Modal MRI/Photoacoustic Imaging Guided Photothermal Therapy of Cancer. *Adv. Funct. Mater.* **2015**, *25*, 1451-1462.

(29) Guo, M.; Mao, H. J.; Li, Y. L.; Zhu, A. J.; He, H.; Yang, H.; Wang, Y. Y.; Tian, X.; Ge, C. C.; Peng, Q. L.; Wang, X. Y.; Yang, X. L.; Chen, X. Y.; Liu, G.; Chen, H.

B. Dual Imaging-Guided Photothermal/Photodynamic Therapy Using Micelles. *Biomaterials* **2014**, *35*, 4656-4666.

(30) Chen, R.; Wang, X.; Yao, X. K.; Zheng, X. C.; Wang, J.; Jiang, X. Q. Near-IR-Triggered Photothermal/Photodynamic Dual-Modality Therapy System via Chitosan Hybrid Nanospheres. *Biomaterials* **2013**, *34*, 8314-8322.

(31) Alric, C.; Taleb, J.; Le, D. G.; Mandon, C.; Billotey, C.; Le, M. A.; Brochard, T.; Vocanson, F.; Janier, M.; Perriat, P.; Roux, S.; Tillement, O. Gadolinium Chelate Coated Gold Nanoparticles As Contrast Agents for Both X-ray Computed Tomography and Magnetic Resonance Imaging. *J. Am. Chem. Soc.* **2008**, *130*, 5908-5915.

(32) Yang, H. W.; Hua, M. Y.; Liu, H. L.; Huang, C. Y.; Tsai, R. Y.; Lu, Y. J.; Chen, J. Y.; Tang, H. J.; Hsien, H. Y.; Chang, Y. S.; Yen, T. C.; Chen, P. Y.; Wei, K. C. Self-Protecting Core-Shell Magnetic Nanoparticles for Targeted, Traceable, Long Half-Life Delivery of BCNU to Gliomas. *Biomaterials* **2011**, *32*, 6523-6532.

(33) Rengan, A. K.; Kundu, G.; Banerjee, R.; Srivastava, R. Gold Nanocages as Effective Photothermal Transducers in Killing Highly Tumorigenic Cancer Cells. *Part. Part. Syst. Charact.* **2014**, *31*, 398-405.

(34) Roy, R. Syntheses and Some Applications of Chemically Defined Multivalent Glycoconjugates. *Curr. Opin. Struct. Biol.* **1996**, *6*, 692-702.

(35) Chen, J.; Huang, L. Q.; Lai, H. X.; Lu, C. H.; Fang, M.; Zhang, Q. Q.; Luo, X. T. Methotrexate-Loaded PEGylated Chitosan Nanoparticles: Synthesis, Characterization, and *in Vitro* and *in Vivo* Antitumoral Activity. *Mol. Pharm.* **2014**, *11*, 2213-2223.

(36) Yuan, F.; Dellian, M.; Fukumura, D.; Leunig, M.; Berk, D. A.; Torchilin, V. P.; Jain R. K. Vascular Permeability in a Human Tumor Xenograft: Molecular Size Dependence and Cutoff Size. *Cancer Res.* **1995**, *55*, 3752-3756.

(37) Karakoti, A. S.; Das, S.; Thevuthasan, S.; Seal, S. PEGylated Inorganic Nanoparticles. *Angew. Chem. Int. Ed.* **2011**, *50*, 1980-1994.

(38) Xia, Y. and Halas, N. J. Shape-Controlled Synthesis and Surface Plasmonic Properties of Metallic Nanostructures. *MRS Bull.* **2005**, *30*, 338-348.

(39) Kakkar, D.; Dumoga, S.; Kumar, R.; Chuttani, K.; Mishra, A. K.; PEGylated Solid Lipid Nanoparticles: Design, Methotrexate Loading and Biological Evaluation in Animal Models. *Med. Chem. Commun.* **2015**, *6*, 1452-1463.

(40) Zhu, J. Y.; Zheng, L. F.; Wen, S. H.; Tang, Y. Q.; Shen, M. W.; Zhang, G. X.; Shi, X. Y. Targeted Cancer Theranostics using Alpha-Tocopheryl Succinate Conjugated Multifunctional Dendrimer-Entrapped Gold Nanoparticles. *Biomaterials* **2014**, *35*, 7635-7646.

(41) Li, Z. W.; Yin, S. N.; Cheng, L.; Yang, K.; Li, Y. G.; Liu, Z. Magnetic Targeting Enhanced Theranostic Strategy Based on Multimodal Imaging for Selective Ablation of Cancer. *Adv. Mater.* **2014**, *24*, 2312-2321.

Table of Contents Image